High-resolution 2D Raman mapping of mono- and bicomponent filament cross-sections

E. Perret [a,b,*,1], O. Braun [c,d,1], K. Sharma [a,e], S. Tritsch [a,f], R. Muff [c], R. Hufenus [a]

[a] Laboratory for Advanced Fibers, Empa, Swiss Federal Laboratories for Materials Science and Technology, Lerchenfeldstrasse 5, 9014, St. Gallen, Switzerland
[b] Center for X-ray Analytics, Empa, Swiss Federal Laboratories for Materials Science and Technology, Überlandstrasse 129, 8600, Dübendorf, Switzerland
[c] Transport at Nanoscale Interfaces Laboratory, Empa, Swiss Federal Laboratories for Materials Science and Technology, Überlandstrasse 129, 8600, Dübendorf, Switzerland
[d] Department of Physics, University of Basel, Klingelbergstrasse 82, 4056, Basel, Switzerland
[e] KTH Royal Institute of Technology, Stockholm, 114 16, Sweden
[f] Hochschule Reutlingen, Alteburgstrasse 150, 72762, Reutlingen, Germany

ARTICLE INFO

ABSTRACT

A high-resolution Raman mapping method has been developed in order to obtain 2D information about structural anisotropies (crystallinity, molecular alignment) in thin filament cross-sections (diameters between 27 μm and 79 μm). Cross-sections of melt-spun, hot-drawn poly (ethylene terephthalate) (PET) filaments and bicomponent core-sheath PET-polyamide 6 (PA6) filaments have been scanned through a laser beam (spatial resolution <1 μm). Raman spectra were analyzed with a specifically developed peak fitting method to obtain Raman maps, e.g., mapped peak height ratios across the face of the fibers. These maps reveal microscopic interconnected networks of crystalline strands within a low crystalline matrix. Radial gradients in PET crystallinity, as well as average and surface crystallinities, were determined. The presented Raman mapping method to visualize variations in the PET crystallinity across such fine filament cross-sections, and the findings thereof, open a new pathway to better understand how fiber processing parameters affect radial fiber structures.

1. Introduction

Among synthetic fibers, poly (ethylene terephthalate) (PET) fibers have the highest production volume worldwide and are widely used in sectors like automotive, furnishing, homewear, sportswear, technical wear amongst other sectors [1]. Structural properties like molecular orientation, crystallite sizes and crystallinity strongly influence the mechanical properties such as tensile strength, elongation at break, abrasion resistance and shrinkage of semi-crystalline fibers [2]. To optimize and tailor physical fiber properties, it is, therefore, crucial to study the interplay between processing parameters and structural changes ranging from the molecular to the microscopic level [3]. Typically, structural studies on fibers focus on comparing average quantities like crystallinity, molecular orientation, long-spacing or crystallite sizes, extracted from e.g. wide-angle x-ray diffraction (WAXD) or small-angle x-ray scattering (SAXS) patterns [4–7].

However, of particular interest for technical textiles is the detailed microscopic 2D structure (crystallinity, molecular alignment) of polymer fiber cross-sections, since it strongly influences the mechanical properties and affects the surface characteristics of the fibers. For example, radial gradients in, e.g., molecular orientation or crystallinity can strongly affect the abrasion resistance of polymer fibers [8]. It is, however, very challenging to obtain 2D structural information across polymer filament cross-sections with diameters below e.g. 80 μm. Some methods exist to obtain radial average structural (e.g., crystallinity or molecular alignment) gradients in filaments, e.g., one-dimensional WAXD tomography [9–13] or polarized light microscopy [14], but these methods do not provide 2D structural information across the face of the fiber. Other methods to study microscopic structural features in polymers are for example atomic force infrared (AFM-IR) mapping [15–17].

Recently, confocal Raman mapping has become a very attractive

---

technique to elucidate changes in the chemical composition in polymer blends [18,19] or in the structure of various materials [20,21]. Confocal Raman spectroscopy has also been used to study the core of a PET-polypropylene (PP) core/sheath fiber by focusing the laser to the center of the fiber through the PP sheath [22]. The disadvantage of focusing the laser through the sheath to the core of the fiber is that the spectrum of the PET core is overlapping with some remaining peaks from the PP sheath, making it rather challenging to obtain radial gradients in this way.

In this work, we present a newly developed high-resolution (spatial resolution <1 μm) 2D Raman mapping method to study the 2D structure of thin polymer filament cross-sections (diameters <79 μm). The structure of monocomponent PET and bicomponent PET-polyamide 6 (PA6) core/sheath filament cross-sections was analyzed with Raman mapping and wide-angle x-ray diffraction (WAXD). For the Raman mapping, a special embedding and polishing technique of fibers was employed. A respective fitting algorithm was developed to analyze structural differences, like anisotropies in crystallinities or molecular alignment, between i) PET filaments which have been drawn offline with different draw ratios and between ii) a melt-spun bicomponent PET-PA6 (core-sheath) filament and a PET monocomponent filament. Extracted surface crystallinity and average crystallinity values from the Raman maps have been validated with other methods, such as attenuated total reflection Fourier transform infrared spectroscopy (ATR-FTIR), WAXD and differential scanning calorimetry (DSC), respectively. Descriptions of the ATR-FTIR and DSC measurements and analysis procedures are given in the data in brief [23]. SAXS was also performed to confirm the presence of crystals in the PET material and to estimate crystal long-spacings and crystallite sizes. Results thereof are shown in the data in brief [23].

2. Experimental

2.1. Materials

Three PET monofilaments were studied, which are labeled DR1, DR2 and DR4. A melt-spun amorphous PET fiber (DR1), which was directly wound up after melt-spinning (speed 600 m/min) without drawing, was provided by Monosuisse AG (Emmenbrücke, Switzerland). This filament was melt-spun from PET polymer pellets from Invista (Wichita, Kansas, United States), which had an intrinsic viscosity of about 0.63 dl/g. A spinneret die with a 0.45 mm opening was used. This as-spun fiber was used as provided to produce two post-drawn fibers (DR2 and DR4) with draw ratios 2 and 4, respectively. The draw ratios represent the ratios between speeds of take-up godet and winder. The offline drawing was performed at Empa (St. Gallen, Switzerland) with a custom-made drawing setup using three godets and a heating plate [23] (section 2.2).

In addition, bicomponent PET-PA6 (core-sheath) filaments, as well as a monocomponent PET multifilaments were produced via direct spinning using a custom-made pilot plant at Empa (St. Gallen, Switzerland). The melt-spinning plant is described elsewhere [24], but detailed spinning parameters are given in section 2.3. The studied single filaments out of multifilaments are named (bico) for the bicomponent PET (core)-PA6 (sheath) fiber and (mono) for the melt-spun PET monocomponent filament. These (bico) and (mono) filaments were melt-spun using post-condensated PET polymer pellets. During post-condensation, the molecular weight of PET was increased by applying heat under vacuum until an intrinsic viscosity of about 0.79 dl/g was achieved (Serge Ferrari Tersuisse AG, Emmen, Switzerland). PA 6 pellets (Grilon F34 natur, M_n = 25–80 kDa, M_w = 50–54 kDa) were used as raw material for the sheath of the bico fiber and have been obtained from Ems-Chemie AG (Domat/Ems, Switzerland). Draw ratios, fineness and diameters of all single filaments are summarized in Table 1.

Table 1

Draw ratios, single filament fineness and diameters.

Fiber label	Draw ratio, DR	Fineness of single filaments (tex = mg/m)	Diameter[a] (μm)
DR1	as-spun	7.20	79
DR2	2.0	3.48	56
DR4	4.1	1.78	44
mono	4.0	0.84	27
bico	4.0	0.71	d_{fiber} = 29 d_{core} = 23

[a] Determined from Raman maps.

2.2. Offline drawing of PET fibers

Fiber DR1 was used as received and was drawn with draw ratios 2 and 4 to fibers DR2, DR4 using the following procedure. The drawing was carried out on an in-house assembly at Empa (St.Gallen, Switzerland) consisting of three godets and a winder along with a few guide rollers and a heating plate [23]. A first minor drawing occurred between godet 1 and godet 2, which was carried out at room temperature (20 °C). The major drawing, however, took place between godet 2 and 3, where the fiber was directed over a heating plate which was placed between these two godets. The heating plate was maintained at 170 °C and was kept at a distance of about 2 mm from the filament. Godet 3 was maintained at room temperature (20 °C) and the final minor drawing took place between godet 3 and the winder. Table 2 summarizes the drawing parameters for fibers D2 and DR4.

2.3. Melt-spinning of bicomponent PET-PA6 and PET filaments

The following multifilaments were melt-spun at Empa: bicomponent PET-PA6 multifilaments (bico) and PET monocomponent multifilaments (mono). Prior to spinning, the PET and PA6 pellets were dried under vacuum for 8 h at 100 °C. For the bicomponent filaments, the PET pellets were melted with an 18 mm, and the PA6 pellets with a 13 mm single screw extruder, each with a length to diameter ratio of 25. The extruder pressures needed for an effective operation of the melt pumps were set to 80 bar, and the throughputs were set to 3 cm³/min for PET and 1.5 cm³/min for PA6. Here, the given throughput values are only nominal values. The effective throuputs, that determine the volume ratio between the core and the sheath material, may slightly differ from the given values due to pressure differences over the pump or other reasons. Three heating zones were used in the extruder, which increased from 250 to 270 °C for PET and from 240 to 260 °C for PA6. The spin pack temperature was set to 270 °C. For core-sheath bicomponent spinning, a spinneret with seven multiple dies [3], each comprising a core capillary with 0.40 mm inner diameter and 0.55 mm outer diameter within a 0.71 mm nozzle. For the monocomponent multifilaments, the same spinneret was used, but no PA6 was added and a higher throughput was chosen (4.5 cm³/min) for the PET. The polymer melt leaving the spinneret was quenched in a 1.2 m long air cooling chamber at 14 °C. Three godets were used to draw the polymer melt directly after the air cooling

Table 2

Drawing parameters for DR2 and DR4. The numbers in parenthesis along with the speeds represent the number of windings on the respective godets.

Fiber label	Godet 1 (at 20 °C) speed (m/min)	Godet 2 (at 95 °C) speed (m/min)	Heating plate temperature (°C)	Godet 3 (at 20 °C) speed (m/min)	Winder speed (m/min)	Draw ratio
DR2	70 (6w)	71 (2w)	170	140 (6w)	142	2.03
DR4	70 (6w)	71 (2w)	170	280 (6w)	285	4.07

chamber (online drawing). Godet temperatures, speeds and number of windings are given in Table 3. The speeds were chosen to be the same for both multifilaments (bico and mono), but the godet temperatures for the mono fiber had to be slightly different to achieve a stable process for the drawing of the filaments.

Single filaments out of the sevenfold melt-spun multifilaments have been investigated with Raman mapping. The other techniques, DSC, WAXD and SAXS were performed on filament bundles. For DSC, WAXD and SAXS, the PA6 sheath of the bico filament was removed with the following procedure: The filament bundles were wound around a specially designed 3D printed holder and were immersed in a solvent mixture comprising 3 parts of formic acid (>99%) and 2 parts of dichloromethane (99.9%) [25]. The setup was maintained at room temperature for 1 h while being continuously stirred with a magnetic stirrer at 250 rpm. Later, the fiber bundles were washed multiple times with water and acetone to completely get rid of the remnant solvent mixture and were subsequently left to dry in air.

2.4. Characterization

2.4.1. High-resolution Raman mapping

The fibers were embedded in a resin hardener (Epoxi cure 2, Buehler, USA) in order to measure Raman maps of polished fiber cross-sections. Fibers were wound on a sample holder and subsequently embedded under vacuum in order to avoid air inclusions. The samples were cured overnight and further ground and polished several times in order to obtain a smooth and transparent surface for subsequent Raman spectroscopy measurements [23].

Raman spectra were acquired using a WITec Alpha 300 R confocal Raman microscope (WITec GmbH, Ulm, Germany) in backscattering geometry. As an excitation source, a laser with 488 nm wavelength was used. The light was focused onto the embedded sample using a $100\times$ objective with a numerical aperture of 0.9, resulting in a diffraction-limited in-plane laser spot size of <1 μm. The confocality of the Raman microscope limits the focal depth to approximately <1 μm. The Rayleigh scattered light was blocked by a notch filter. The backscattered light was coupled to a 300 mm lens-based spectrometer with a grating of 1800 g/mm for all filaments. The spectrometer is equipped with a thermoelectrically cooled CCD (1600×200 pixel, pixel size 16×16 μm^2) leading to a spectral resolution of <0.85 cm^{-1}. Raman spectra were acquired with a set laser power of 1 mW and an integration time of 2.0 s for the mono and bico filaments, and a laser power of 5 mW with an integration time of 0.4 s for DR1, DR2 and DR4, respectively.

The embedded samples were mounted on a piezo stage and maps of fiber cross-sections were acquired by scanning the sample through the laser. The raw spectra have been treated with a cosmic ray removal procedure and a background was subtracted using a moving shape with a radius of 100 cm^{-1} in order to remove signatures of photo-luminescence. All corrected Raman spectra were subsequently binned by averaging over 4 spectra (2×2), spanning an area of 1 μm^2. Before fitting, the binned spectra were all normalized by the intensities of the 1291 cm^{-1} Raman band. This normalization was necessary in order to account for changes in the absolute intensity due to a slightly bent fiber surface, which we have observed with atomic force microscopy [23].

Spectral analysis was done with specially developed Python codes, where Raman peaks of interest were fit with one or two Pearson VII functions and a linear background. A Pearson VII function is a Lorentzian function raised to the power *m* and is given by the following equation.

$$I_{sim}^{Raman} = I \frac{FWHM^{2m}}{\left[FWHM^2 + \left(2^{1/m} - 1\right)\left(x - x_0\right)^2\right]^m} \qquad \text{(Eq. 1)}$$

The peak height is *I*, and the full width at half maximum is given by *FWHM*, *x* is the Raman shift and x_0 is the Raman shift peak position. The shape factor, *m*, was fixed for each map, but varied from map to map in order to enable a better fitting of different tail-shapes of peaks of interest in individual samples. For almost all peaks and samples, shape factors between 1 and 12 were found to lead to best fitting errors. In general, different peak shapes are only slightly improving fits but are not significantly affecting the final results of the Raman maps.

2.4.2. Wide-angle X-ray diffraction (WAXD)

WAXD were recorded on a Bruker Nanostar U diffractometer (Bruker AXS, Karlsruhe, Germany) with a Cu-Kα radiation λ = 1.5419 Å and a VÅNTEC-2000 MikroGap area detector. Single filaments (DR1, DR2, DR4) or fiber bundles (mono, bico, bico with sheath removed) were mounted on sample holders for WAXD, and the sample to active detector area distance was about 9.3 cm. The recorded patterns were analyzed with the evaluation software DIFFRAC.EVA (version 4.2., Bruker AXS, Karlsruhe, Germany) and specifically developed Python codes. For the samples, DR4, mono and bico with sheath removed, the crystallinity values of PET (percentage of crystalline intensity in WAXD patterns) were estimated from Lorentz corrected 2D patterns by analyzing azimuthal and radial profiles using DIFFRAC.EVA [23]. The Lorentz correction has been explained elsewhere [26]. SAXS patterns have also been collected and are shown in the data in brief [23].

3. Results and discussion

3.1. Raman analysis

Raman maps were measured with 180x180 lines over 90×90 μm for DR1, with 140×140 lines over 70×70 μm for DR2, with 100×100 lines over 50×50 μm for DR4 and with 70×70 lines over 35×35 μm for the PET monocomponent (mono) fiber and PET-PA6 bicomponent fiber (bico) with 0.5 μm steps. Microscope images of the cross-sections that were taken with the Raman setup are shown in the data in brief [23].

Raman spectra at the center (each averaged over 9 (3x3) spectra from an area of 1.5×1.5 μm) of all fiber cross-sections are shown in Fig. 1. A Raman spectra of the surrounding epoxy material and of PA6 are shown at the bottom of Fig. 1. As expected, vibrations of different functional groups in PET and PA6 in the bicomponent fiber lead to distinct peaks in the Raman spectrum, and the materials can easily be distinguished from one another. For PA6 we have analyzed the peak at 1635 cm^{-1}, which can be assigned to the C=O amide stretching [27].

All Raman spectra from PET have been normalized to the peak at 1291 cm^{-1} (ring and O–C stretching [28]), since this band has shown a rather constant intensity.

Multiple research groups have shown that the ethylene glycol segment of PET adopts a *trans* conformation in the crystalline phase, whereas both *gauche* and *trans* conformations are present in the amorphous phase [28–35]. These conformations lead to specific Raman [28–35] and infrared bands [36–40], which may be used to determine PET crystallinities [36,41,42]. The *trans* conformation gives rise to a peak at 1095 cm^{-1} [28–30,41,43] and the *gauche* conformation gives

Table 3

Processing parameters of PET-PA6 bicomponent and PET multifilaments. Number of windings around godets are indicated in brackets.

Fiber label	Godet 1 temperature (°C)	Godet 1 speed (m/min)	Godet 2 temperature (°C)	Godet 2 speed (m/min)	Godet 3 temperature (°C)	Godet 3 speed (m/min)	Winder speed (m/min)
bico	125	250 (4w)	60	990 (8w)	40	1000 (5w)	990
mono	100	250 (6w)	80	990 (10w)	40	1000 (5w)	990
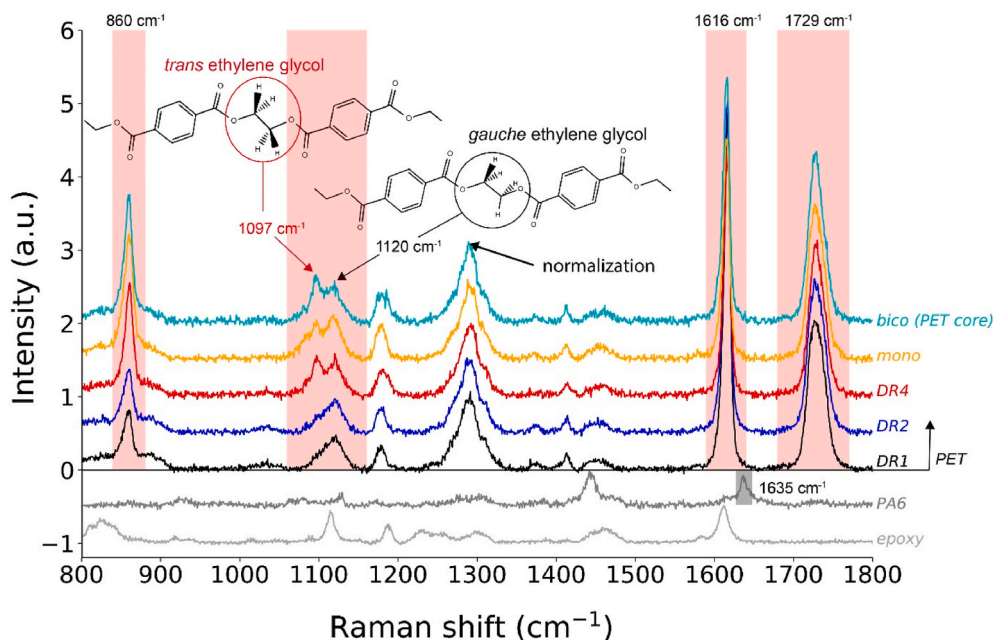
Fig. 1. Raman spectra from PET in the center of all fiber cross-sections (DR1, DR2, DR4, mono, bico) as well as of the surrounding epoxy material and the PA6 sheath of the bicomponent sample. The investigated Raman bands are highlighted in red and gray respectively. (For interpretation of the references to colour in this figure legend, the reader is referred to the Web version of this article.)

rise to a peak at 1120 cm⁻¹ (inset in Fig. 1). Significant differences in peak heights in the Raman spectra of the PET fiber cores are mainly visible at 860 cm⁻¹, 1097 cm⁻¹ and 1616 cm⁻¹, and the width of the 1729 cm⁻¹ band is also changing with increasing draw ratio.

Table 4 summarizes some characteristic vibrational bands of PET (shaded in red in Fig. 1), which have been studied in this work.

For the PET material, four spectral regions around (860, 1110, 1616, 1729 cm⁻¹) were fitted with Pearson VII functions (shaded areas in Fig. 1), as explained in the experimental section. Fitting examples of binned spectra at the center of all measured fiber cross-sections are given in Fig. 2.

In total, 32041 (179×179) binned spectra were fit for DR1, 19321 (139×139) for DR2, 9801 (99×99) for DR4 and 4761 (69×69) for the (mono) and (bico) fibers. Average peak positions, peak widths and peak height ratios, which were obtained by averaging the fitting parameters over the entire fiber cross-sections, are summarized in Table 5. Note that the calculated standard errors of average peak widths and positions are below 0.1 cm⁻¹. These standard errors, $\overline{\Delta x}$, are calculated from fitting errors, Δx_i, of N binned spectra in the fiber cross-sections, by taking into account the error propagation, $\overline{\Delta x} = \frac{1}{N}\sqrt{\sum_{i=1}^{N} \Delta x_i^2}$. Peak height ratios were calculated by dividing the individual peaks by the measured peak intensity of the 1120 cm⁻¹ peak that arises from *gauche* conformations in the amorphous phase. Complete maps of specific Raman peak positions, widths, heights, areas, height ratios and area ratios for all fibers are

shown in the data in brief [23].

3.1.1. Peak positions

Upon drawing of fiber DR1, the peak at 858.3 cm⁻¹ shifts to a slightly larger value, 860.1 cm⁻¹, by (Δpos.~ +1.8 cm⁻¹), while the 1100.8 cm⁻¹ shifts to a smaller value, 1097.2 cm⁻¹ (Δpos.~ −3.6 cm⁻¹). Wavenumber shifts are typically correlated with changes in the bond length and thus the interatomic force constants [46,47]. A shift towards higher wavenumber is typically caused by a shortening of bond lengths, and a shift towards lower wavenumbers by a lengthening of bond lengths. Thus, the observed peak shifts upon drawing may relate to conformational changes that occur when chains in the amorphous phase become more stretched or start to form crystals with neighboring chains.

The peak positions for the PET core in the bicomponent fiber are all very similar to the ones of the monocomponent fiber, which may signify that there are no significant differences in the bond lengths between these samples.

3.1.2. Peak widths

Maps of the full width at half maximum of specific Raman peaks are shown in the data in brief [23] for all fibers. Overall, the FWHMs of all the peaks related to the PET material are the smallest for DR4 but are slightly increased for DR2 with respect to DR1 (Table 5). The width of the Raman band at around 1729 cm⁻¹ (C = O stretching) is changing from as-spun (DR1) to drawn fibers (DR4) (ΔFWHM ~ −2.3 cm⁻¹). Changes in the width of this Raman band have been associated with changes in crystallinity, density or conformations in the past [28–30]. A sharp peak (small FWHM₁₇₂₉) has typically been correlated with a higher density. For the bico fiber, the FWHMs of the 1097 cm⁻¹ and 1729 cm⁻¹ are rather small compared to the mono fiber (ΔFWHM -17.7 cm⁻¹ and -1.8 cm⁻¹, respectively), which we hence interpret as a sign that the PET core in the bico fiber has a higher density.

The peak widths of the mono fiber are comparable to peak widths somewhere between DR2 and DR4, except the width of the 1097 cm⁻¹ peak, which is significantly larger (up to ΔFWHM ~ +17.7 cm⁻¹) than for all other fibers. The latter could indicate that there is a larger poly-dispersity in the ethylene glycol C–C bond lengths in the crystalline phase of the melt-spun mono fiber. We have also performed WAXD

Table 4
Assignments of Raman peaks to vibrations in PET [28,29,34,44].

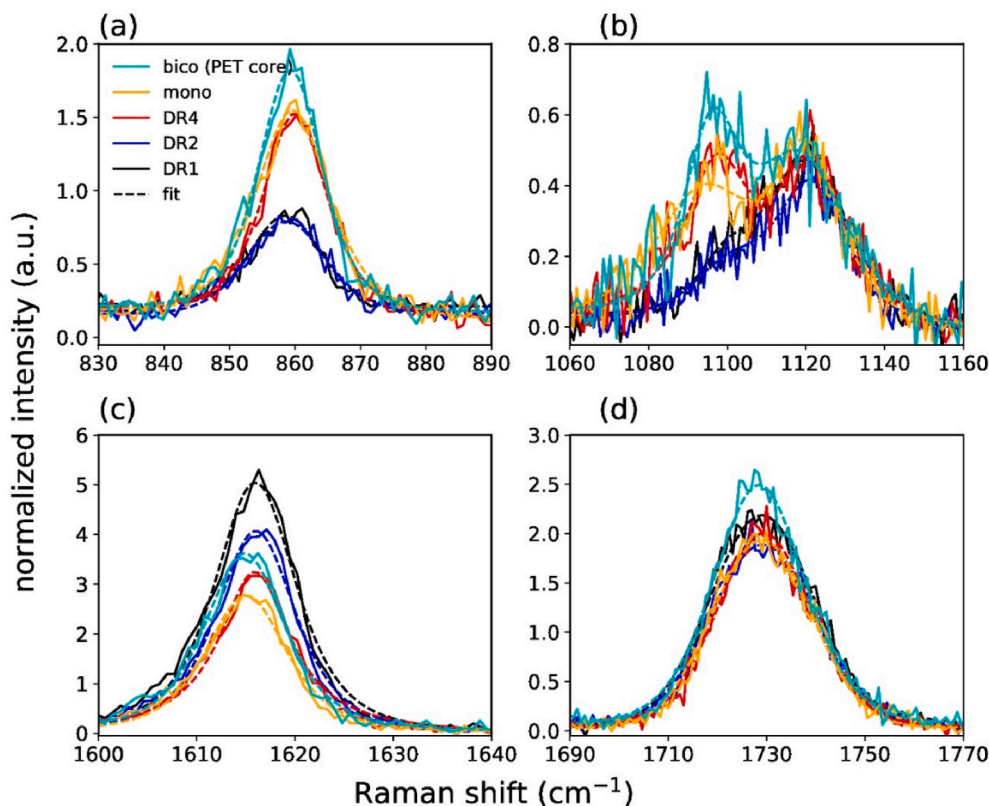| Peak position	Assignment
860 cm⁻¹	Ring C–C breathing (A_g mode), ester C(O)–O stretching
1097 cm⁻¹	Ring C–C, ester C(O)–O, ethylene glycol C–C stretching (*trans*)
1120 cm⁻¹	Ring C–H in-plane bending, ester C(O)–O and ethylene glycol C–C stretching (*gauche*)
1291 cm⁻¹	Ring and O–C stretching (used for normalization)
1616 cm⁻¹	C–C/C = C benzene ring mode 8a (Wilson notation [45])
1729 cm⁻¹	C=O stretching

Fig. 2. Fits and measured Raman spectra of PET at the center of the fibers. Dashed curves: fits. Solid curves: 2x2 binned measured spectra.

Table 5
Extracted average peak positions, full width at half maximum (FWHM) and height ratios of individual peaks with respect to the peak at 1120 cm^{-1} for the cross-sections of all fibers. Standard errors are smaller than 0.1 cm^{-1}.

	DR1	DR2	DR4	mono	bico
Position (cm^{-1})	858.3	858.6	860.1	859.7	859.3
FWHM (cm^{-1})	12.7	13.0	11.4	12.9	11.5
I_{860}/I_{1120}	1.4	1.5	2.8	3.1	3.2
A_{860}/A_{1120}	0.7	0.7	1.2	2.1	1.6
Position (cm^{-1})	1100.8	1100.2	1097.2	1095.1	1096.2
FWHM (cm^{-1})	16.9	18.5	14.6	32.1	15.3
I_{1097}/I_{1120}	0.4	0.4	1.0	0.8	1.1
A_{1097}/A_{1120}	0.3	0.3	0.6	1.4	0.8
Position (cm^{-1})	1121.0	1120.9	1120.4	1118.8	1118.2
FWHM (cm^{-1})	25.2	24.9	23.7	19.3	22.0
I_{1120}	0.4	0.4	0.5	0.5	0.4
A_{1120}	12.7	12.7	15.6	11.3	11.8
Position (cm^{-1})	1616.0	1616.0	1615.9	1615.0	1615.0
FWHM (cm^{-1})	9.5	9.6	8.9	9.7	9.7
I_{1616}/I_{1120}	11.7	11.1	8.0	6.4	7.3
A_{1616}/A_{1120}	4.6	4.4	3.2	3.2	3.2
Position (cm^{-1})	1729.0	1729.0	1729.4	1728.9	1728.6
FWHM (cm^{-1})	25.0	25.0	22.7	23.9	22.2
I_{1729}/I_{1120}	4.9	4.9	4.6	4.3	4.9
A_{1729}/A_{1120}	4.4	4.4	3.4	4.7	4.5

measurements which indicate that the mono fiber contains a significant amount of a non-crystalline mesophase [4,5,40,48–51,81], made of highly oriented and stretched PET macromolecules along the fiber axis. A larger polydispersity in the ethylene glycol C–C bond lengths could thus also be explained by the presence of this mesophase, which is further discussed in the WAXD section 3.2.
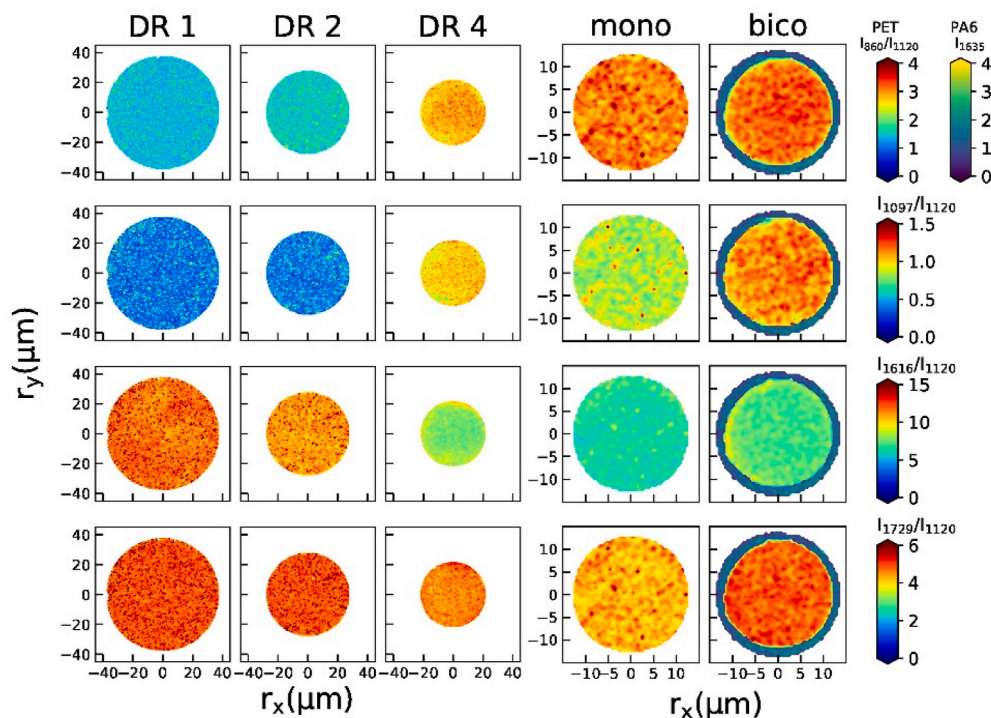
3.1.3. Peak height ratios

Maps of peak height ratios (I_{peak}/I_{1120}) with respect to the *gauche* peak at 1120 cm^{-1} (amorphous) are shown in Fig. 3.

All maps reveal interconnected networks of microscopic strands of high crystallinity within a low crystalline matrix. Note that corresponding maps from peak area ratios are given in the data in brief [23]. These maps also show very similar interconnected networks. As mentioned before, changes in the intensity can be attributed to changes in density, crystallinity or conformations. Especially, the ratio I_{1097}/I_{1120} can directly be correlated with density changes. Note that, we discuss the extraction of radial profiles of crystallinity values and average crystallinities in subsection 3.1.5.

The average peak height ratios I_{860}/I_{1120} and I_{1097}/I_{1120} are increasing by a factor of two (Table 5) upon drawing (from DR1 to DR4). The latter occurs due to conformational changes from *gauche* to *trans* of ethylene glycol segments. Peak height ratios I_{1616}/I_{1120} and I_{1729}/I_{1120} are however decreasing in intensity upon drawing (from DR1 to DR4). The peak height ratio I_{1616}/I_{1120} is the smallest for the mono filament and is also rather small for the bico filament. The peak at 1616 cm^{-1} is assigned to the symmetric stretching of the 1,4-carbons of the benzene ring [52] and is reflecting the molecular orientation of polymer chains [43,52–54]. Since the incident light onto the sample is linearly polarized in the plane of the sample (fiber cross-section), only benzene rings that lie fully or partially in the plane of the fiber cross-section will contribute to the 1616 cm^{-1} Raman band. Thus, a decrease in the 1616 cm^{-1} peak intensity in the fiber cross-section upon drawing indicates that there are more benzene rings aligned towards the drawing direction in highly drawn fibers, which is also in accordance with a higher molecular orientation [43,55]. Therefore, we conclude that the highly drawn samples, DR4, mono and bico, have a rather high molecular orientation.

3.1.4. Correlations within the cross-sections of individual fibers

In order to investigate the correlations within the fiber cross-sections of individual samples, we have made correlation plots, where peak

Fig. 3. Peak height ratios of individual peaks (860 cm^{-1} (first row), 1097 cm^{-1} (second row), 1616 cm^{-1} (third row), 1729 cm^{-1} (forth row)) with respect to the 1120 cm^{-1} peak, mapped across all fiber cross-sections.

height ratios and the FWHM of the 1729 cm^{-1} peak are plotted against the peak height ratios I_{1097}/I_{1120}. Fig. 4 summarizes the correlation plots for all samples. Corresponding 2D correlation maps are shown in the data in brief [23].

The peak height ratio I_{1097}/I_{1120} correlates with the density/

crystallinity of the samples and has therefore been chosen as the x-axis in the plots. The numbers given in the top left corner of each correlation plot correspond to the calculated Pearson correlation coefficients (PCC) of the compared variables over the entire fiber cross-section. A value of 1 signifies a total positive linear correlation, 0 signifies no linear
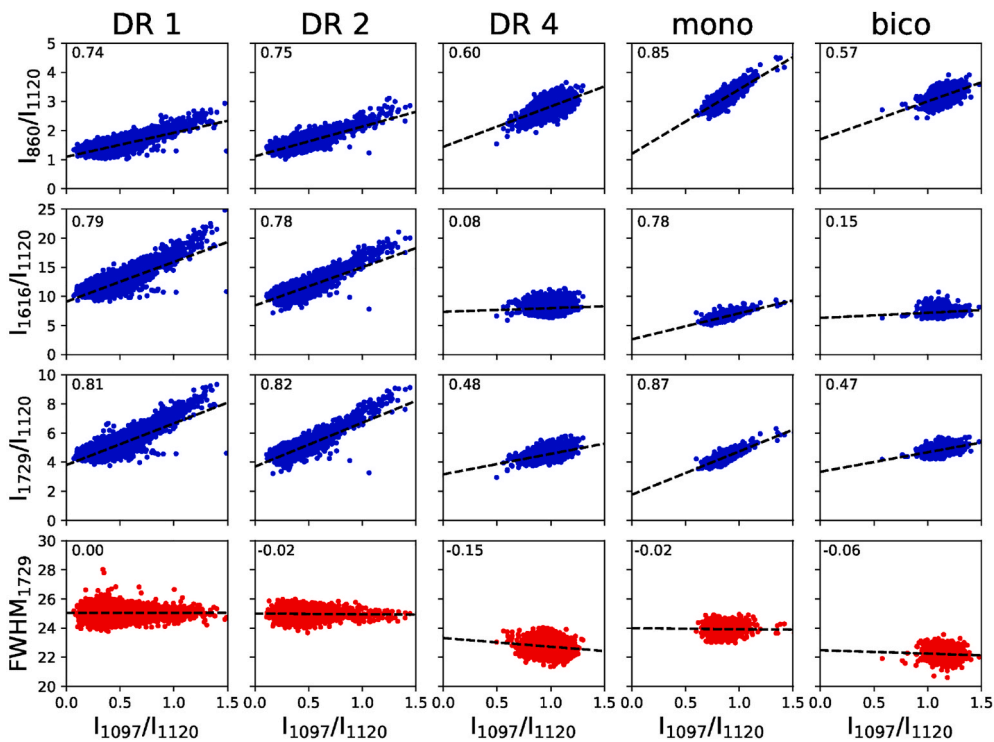
Fig. 4. Correlations between peak height ratio I_{1097}/I_{1120} and the three peak height ratios I_{860}/I_{1120}, I_{1616}/I_{1120}, I_{1729}/I_{1120} as well as FWHM of 1729 cm^{-1} peak for all measured spectra in all fiber cross-sections. Pearson correlation values, PCC, are given in the top left corner of each figure. Dashed lines serve as a graphical representation of the PCC, where their slope corresponds to the PCC.

correlation, and -1 signifies a total negative linear correlation. For DR1, DR2 and mono fibers, all peak height ratios show a positive linear correlation (PCC ≥0.74) with the peak height ratio I_{1097}/I_{1120}, whereas the FWHM of 1729 cm^{-1} is rather constant in all samples and thus shows no linear correlation. For DR4 and the bico fiber, mainly the peak ratios, I_{860}/I_{1120} and I_{1729}/I_{1120}, are positively correlated with I_{1097}/I_{1120}, whereas no or only a small positive linear correlation is observed between I_{1616}/I_{1120} and I_{1097}/I_{1120}. This result suggests that not only the intensity ratio I_{1097}/I_{1120} is reflecting changes in the density/crystallinity within a sample, but also I_{860}/I_{1120} or I_{1729}/I_{1120}, whereas the other ratio, I_{1616}/I_{1120}, is more strongly influenced by molecular orientation, and the FWHM of the 1729 cm^{-1} peak is rather constant within the samples.

3.1.5. Radial gradients in crystallinity and peak ratios

Significant changes have been observed in the region from 1040 to 1160 cm^{-1}. Two bands are visible in this region. The Raman band near 1097 cm^{-1} (stretching of ring C–C, ester C(O)–O and ethylene glycol C–C bonds) increases in intensity upon drawing, due to the transition of *gauche* to *trans* conformation of the ethylene glycol bonds. This change is seen by the differences in the peak height ratio, I_{1097}/I_{1120}, in the Raman maps shown in Fig. 3. Raman spectroscopy has been used in the past to calculate percent crystallinities for various polymers, e.g., polystyrene [56], polypropylene [57], polyethylene [58] or PET [41]. However, changes in the trans and gauche intensity band may not only be attributed to changes in the chain conformation and thus crystallinity, but also to changes in chain packing and molecular chain orientations [33]. Nevertheless, we have still attempted to quantify the crystallinity of the PET fiber cross-sections with Raman spectroscopy, by applying the same equation as Hafsia et al. [41]:

$$\chi^{Raman}(\%) = \frac{I_{1097} - I_{1097a}}{I_{1117} + I_{1097}} \times 100 \qquad \text{(Eq. 2)}$$

where I_{1097} and I_{1117} are the intensities (peak heights) of the 1097 cm^{-1} and 1117 cm^{-1} peaks, respectively, and I_{1097a} is the intensity of the 1097 cm^{-1} vibration band of a 100% amorphous sample. In PET, the *trans* conformation and thus the I_{1097} peak is also present in a 100% amorphous sample, and therefore its intensity contribution, I_{1097a}, has to be subtracted from the intensity contribution of the semi-crystalline sample, I_{1097}. The I_{1097a} was estimated to be about 0.1 from the lower bounds of the I_{1097} peak in the normalized spectra of the DR1 sample. Equation 4 can be applied for each binned spectrum in the fiber cross-section, enabling the determination of average fiber crystallinity and radial crystallinity gradients. Fig. 5a shows crystallinity maps calculated

using this equation for all fiber cross-sections. As already previously observed with peak height ratio maps, these crystallinity maps reveal interconnected networks of crystalline strands within a low crystalline matrix. Here, the crystalline areas originate most likely from clusters of crystalline fibrils. Interestingly, publications that discuss the microscopic interconnected networks in semi-crystalline polymer fibers are scarce. This might be because it is rather difficult to image microscopic crystalline and amorphous domains, especially for thin filament cross-sections. Up to now, polarized optical microscopy [59–62], transmission electron microscopy [63], and atomic force microscopy [64], have mostly been used to image crystalline domains (e.g. spherulites) in polymer films.

In order to calculate the radial gradients, we have averaged the crystallinities in different annuli of 2 μm width for DR1, DR2 and DR4, and of 1.5 μm width for the mono and bico fiber, respectively. The symmetrized radial gradients of the obtained absolute Raman crystallinities are shown in Fig. 5b.

For DR1, DR2 and mono, the crystallinity is slightly increasing towards the fiber surface, whereas for DR4 and the bico fiber, the crystallinity is decreasing towards the fiber surface or towards the interface to PA6, respectively. In case of online drawn monocomponent filaments (mono), the surface region of the fibers is expected to cool down first (since the core is hot due to drawing from the polymer melt), enhancing the molecular orientation and thus stress-induced crystallization in the surface region. For offline drawn fibers, however, a cold fiber is drawn over a heating plate, thus the core of the fiber is drawn at a colder temperature than the surface region, enhancing the stress-induced crystallization in the core, which could explain the higher crystallinity in the core of the offline drawn fiber, DR4.

Additionally, we have averaged all peak height ratios as well as the FWHM of the peak at 1729 cm^{-1} over the different annuli. The corresponding symmetrized radial gradients are shown in Fig. 6 as percentage changes of the ratios, or FWHM, with respect to the values of the inner core (r <4 μm for DR1, DR2 and DR4, and r <2.5 μm for mono and bico, respectively). Radial gradients are mainly observed for DR4 and the bico fibers in the ratios I_{860}/I_{1120} and I_{1097}/I_{1120} (negative gradients), as well as in the I_{1616}/I_{1120} ratio (positive gradient). The latter suggests that the core has a higher molecular orientation in the DR4 and bico fiber than the outer areas of the fiber cross-sections. The average of the FWHM of the 1729 cm^{-1} peak remains almost constant along the radial direction, which confirms our previous observation in the correlation analysis. Interestingly, for DR2, an oscillatory behavior in the intensity ratios is observed along the radial direction. We suspect that this is a result of threadlike crystalline areas that grow from the sheath to the core, as is
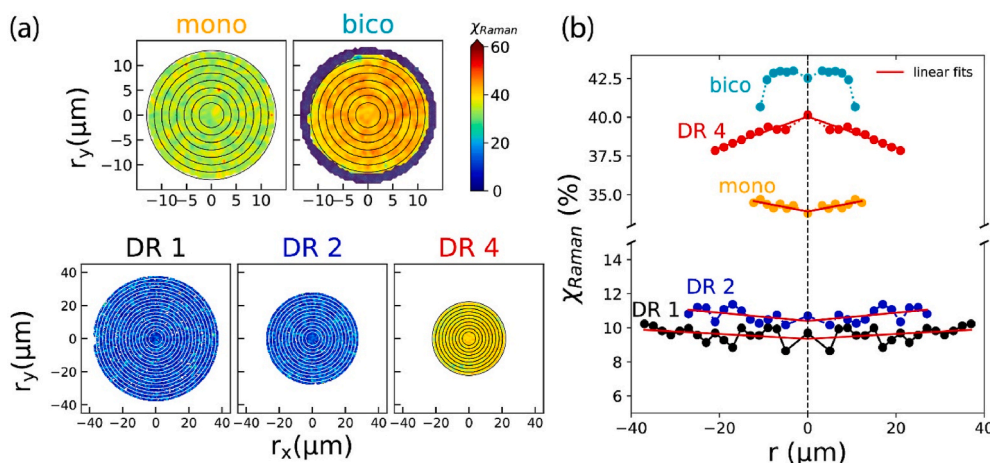
Fig. 5. (a) Calculated Raman crystallinity maps. Top row: mono and bico fibers. Bottom row: DR1, DR2, DR4. Analyzed annuli for radial profiles are illustrated with rings. (b) Symmetrized radial gradients of absolute Raman crystallinity for all fibers. Linear fits are shown as red lines. (For interpretation of the references to colour in this figure legend, the reader is referred to the Web version of this article.)
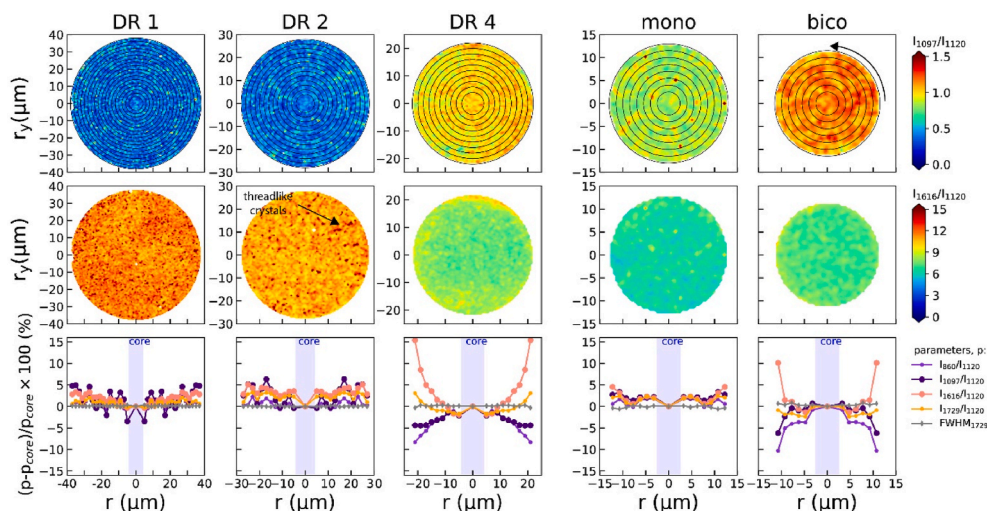
Fig. 6. Top row: peak height ratio maps I_{1097}/I_{1120} with annuli. Middle row: peak height ratio maps I_{1616}/I_{1120}. Bottom row: Symmetrized radial profiles of percentage changes in peak height ratios (I_{860}/I_{1120}, I_{1097}/I_{1120}, I_{1616}/I_{1120}, I_{1729}/I_{1120}) and FWHM of 1729 cm^{-1} peak with respect to the fiber core.

highlighted in Fig. 6 for DR2.

3.1.6. Azimuthal variations

We have also determined the azimuthal change in peak height ratios and FWHM for all fibers, see data in brief [23]. The fiber cross-sections of DR1, DR2 and mono all appear to have a radial symmetry due to the lack of azimuthal changes. DR4 and the bico fiber, however, are not perfectly symmetric. Although the changes in the peak height ratios are rather subtle (<3%), a clear change in certain peak height ratios (I_{860}/I_{1120}, I_{1097}/I_{1120}, I_{1616}/I_{1120}) along the azimuth can be observed, where the relative change in I_{1616}/I_{1120} behaves opposite to the ones of the ratios I_{860}/I_{1120} and I_{1097}/I_{1120}. Fiber DR4 was drawn over a heating plate, which explains why its radial symmetry is not fully given. In the case of the bico fiber, the thickness of the PA6 sheath is not perfectly uniform, which also leads to a breakage of radial symmetry.

3.2. WAXD analysis

As a complementary method, WAXD can be used to determine the phases that are present in the fibers as well as to extract average crystallinity values of the fibers. WAXD patterns of the DR1, DR2, DR4, mono and sheath-removed bico fibers are shown in Fig. 7. Corresponding small-angle x-ray scattering (SAXS) patterns, which give

information about the arrangement of crystals and crystallite sizes, are shown in the data in brief [23]. Note that for the bicomponent fiber, the sheath was removed following the procedure that is explained in the experimental section. WAXD and SAXS patterns of bico fibers still containing the sheath are shown in the data in brief [23]. The scale for the intensity in the patterns is arbitrary, since, for each fiber type, different numbers of fibers have been placed into the x-ray beam.

The WAXD pattern of fiber DR1 shows an amorphous ring. For DR2, we observe an equatorial broad peak, which can be associated with the typical highly oriented non-crystalline mesophase (P_{nc}) in PET [4,5,40, 48–51]. In the literature, various terminologies have been used to describe this phase: liquid crystalline transient mesophase [48,50], taut-tie noncrystalline phase (TTNC) [65], oriented intermediate phase [66], oriented amorphous phase [67], paracrystalline phase [6], and highly oriented non-crystalline mesophase [4,5,51,68–72]. Upon further drawing (DR4), sharp crystalline peaks appear, which arise from the triclinic unit cell of PET [66,73]. The WAXD pattern of the PET core from the bico fiber shows even sharper peaks than the DR4 or mono fiber, confirming a high crystallinity and a high orientation of crystals in the bicomponent fiber. The WAXD pattern of the mono fiber shows that this fiber has a mixture of mesophase and crystalline phase. SAXS patterns confirm that fibers DR1 and DR2 are amorphous (non-crystalline) due to the absence of lamellar reflections. It can, however, not fully be
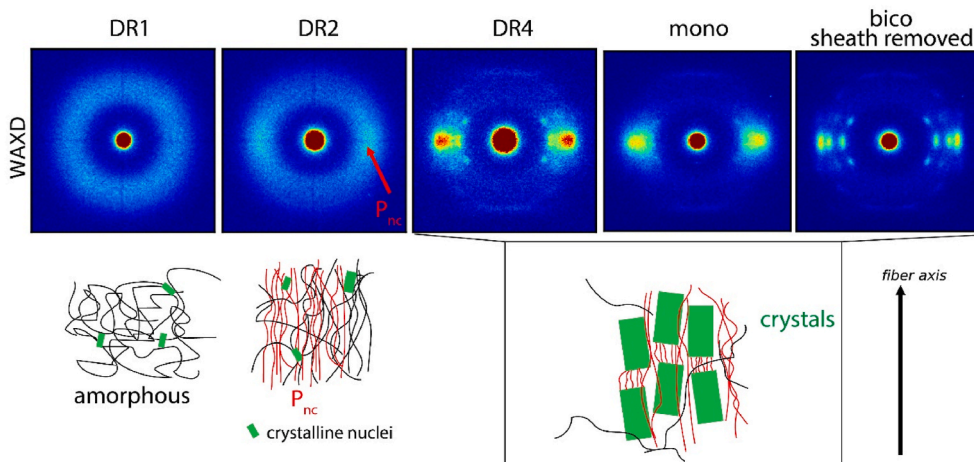
Fig. 7. WAXD patterns for all fibers. Note that for the bicomponent fiber, the sheath was removed. Schematics of corresponding structures are shown in the bottom row.

excluded that there are some small nanocrystals present in these fibers. The presence of the mesophase peak in the WAXD pattern of the DR2 fiber, and the lack of lamellar peaks or rings in the SAXS pattern, indicate that the mesophase is non-crystalline. A sketch of the suggested structures for DR1 and DR2 is shown in the bottom of Fig. 7.

3.3. Comparison of average crystallinity and surface crystallinity values using different methods

Calculated average crystallinity values from Raman mapping of entire fiber cross-sections are summarized in Table 6 and are compared to values obtained by other methods (DSC, WAXD [23]). All average crystallinity values of DSC, WAXD and Raman are remarkably close to each other. The average crystallinities are increasing from DR1 to DR4 due to strain-induced crystallization [74]. Furthermore, the crystallinity of the PET core in the bicomponent fiber is significantly larger than the crystallinity value of the monocomponent PET, which has been melt-spun under almost the same conditions. Only the temperatures of godet 1 and godet 2 have been slightly adapted by $+25\ °C$ and $-20\ °C$, respectively, in order to enable post-drawing of the bicomponent multifilaments with same speeds and DR (Table 3). For the same reason, the number of windings around godet 1 and 2 have been reduced for the bicomponent multifilaments. Although these slight differences in the godet temperatures and number of windings might be responsible for the higher crystallinity of the PET core of the bicomponent filament, we believe that the main reason is because the PA6 sheath slows down the cooling of the PET core. The melting point of PET ($T_m = 260\ °C$) and the glass transition ($T_g = 75\ °C$) are higher than the ones of PA6 ($T_m = 225\ °C$, $T_g = 50\ °C$) [2]. Thus, during solidification, the PET core solidifies first, but its solidification is delayed compared to a PET monocomponent filament without PA6 sheath, since the PA6 sheath stays longer in a molten state due to its lower melting point, which in turn keeps the PET core at elevated temperature for a longer time. Thus, the solidification stress of PET is increased, while that of PA6 is decreased, leading to a higher crystallinity in PET (analogously to PET-PP fibers [75,76]). Note that the thermal conductivity of PET (0.15 $Wm^{-1}K^{-1}$) is significantly smaller than that of PA6 (0.25 $W\ m^{-1}K^{-1}$) at 25 °C [77]. Molecular orientation and crystallinity of the polymer with higher melt and glass transition temperatures (PET) are enhanced, while those of the second polymer (PA6) are suppressed [3]. The higher crystallinity of the PET core in the bicomponent fiber, compared to the monocomponent fiber, can thus be explained by the fact that the radial thermal profile of the PET is influenced by the presence of the surrounding PA6 component. Similar behaviors have been reported in previous publications for PPS-PET (core-sheath) bicomponent fibers [7] and for other bicomponent PET-PA6 fibers [78].

We have also determined the surface crystallinity values of samples DR1-DR3 with attenuated total reflection Fourier transform infrared spectroscopy (ATR-FTIR) (data in brief [23]) and compared the values to the surface crystallinity values extracted from Raman measurements

from the outmost annulus of the fiber cross-sections (Table 6). Extracted crystallinity values from ATR-FTIR spectra are also remarkably close to extracted surface crystallinity values from Raman (see also Figures in data in brief [23]).

However, it turned out that the extraction of crystallinity values from WAXD profiles or ATR-FTIR data is less reliable since the values depend strongly on the selection of the amorphous background. For WAXD, a range of crystallinity values (Table 6, values in brackets) can be obtained, depending on the background selections. In the case of ATR-FTIR, the reference of the amorphous signal contribution to the *trans* infrared bands has to be known, and the pressure applied to the thin fibers may also induce structural changes during the measurement, rendering this method less accurate. Additionally, the estimation of the absorptivity adds another uncertainty to the determination of the surface crystallinity.

4. Conclusion

A high-resolution (spatial resolution <1 μm) Raman mapping method was presented, which enables the study of 2D microstructures (crystallinity and molecular alignment) of thin polymer filament cross-sections. A special peak fitting routine was developed to obtain Raman maps, e.g. peak positions, widths, heights, areas, height ratios and area ratios over the face of polymer fibers. Raman maps have been obtained for differently drawn thin PET filaments (diameter <79 μm) and melt-spun monocomponent PET filaments, as well as bicomponent core-sheath PET-PA6 filaments. Crystallinity values of the PET material were extracted by fitting the Raman spectra peaks arising from the *trans* and *gauche* conformations of the ethylene glycol segment. An interconnected network of microscopic strands of high crystallinity, within a low crystalline matrix, was observed for all fiber cross-sections. Raman, WAXD and DSC data confirmed that the crystallinity increases upon drawing and that the bicomponent PET-PA6 fiber has a more crystalline PET core than the monocomponent melt-spun PET fiber. Crystallinity values in the annuli of the fiber cross-sections were averaged to obtain radial crystallinity profiles. The highly drawn fiber, DR4, and the bicomponent fiber, bico, showed that the PET material was more crystalline in the core than at the PET surface or the PET-PA6 interface. The higher core crystallinity of the offline drawn fiber, DR4, can best be explained by the heating of the fiber from the outside during drawing, whereby the core remains longer cold, which enhances stress-induced crystallization in the core. In case of the bicomponent fiber, the PA6 sheath is supposedly keeping the PET core at elevated temperature for a longer time, leading to a similar effect.

We have shown that high-resolution Raman mapping is an ideal technique to study radial structural gradients in crystallinity or molecular alignments of thin PET fiber cross-sections. A more detailed analysis of the molecular alignments in the fiber cross-sections could be done with polarization-dependent Raman measurements [79,80]. Also, a depth profiling of amorphous and crystalline areas in fiber cross-sections

Table 6
Crystallinity values of PET, obtained with different techniques. NM: not measured, NA: not measurable or not computable.

Sample	Average crystallinity				Surface crystallinity			
	χDSC(a) (%)	χWAXD ($\S$) from azimuthal profiles (%)	χWAXD ($\S$) from radial profiles (%)	χRaman(b) (%)	χsurface Raman(c) (%)	χ_{1340}^{FTIR}(%)	χ_{1475}^{FTIR}(%)
DR1	7.9 ± 1.2	NA	NA	9.7 ± 6.5	10.2 ± 7.2	15.1 ± 2.3	13.6 ± 1.3
DR2	11.4 ± 1.6	13.0^* (10.8–18.1)	NA	10.8 ± 6.0	10.7 ± 6.6	19.6 ± 1.9	16.1 ± 2.5
DR4	36.8 ± 0.6	36.6 (28.2–45.1)	35.8 (24.6–47.8)	38.6 ± 2.7	37.9 ± 3.0	38.3 ± 0.6	34.1 ± 1.4
mono	37.4 ± 0.5	38.9 (34.6–44.2)	38.5 (30.5–47.2)	35.2 ± 3.4	35.5 ± 3.2	NM	NM
bico, PET	40.4 ± 1.7	NA	NA	41.0 ± 2.4	39.3 ± 2.6	NA	NA
bico, sheath removed	41.7 ± 1.1	42.2 (32.1–53.7)	44.6 (38.7–51.9)	NM	NM	NM	NM

($\S$) values in brackets correspond to lower and upper bounds [23]. *This intensity percentage is attributed to the Pnc mesophase. Standard deviations are calculated from: (a) three DSC measurements. (b) all measured crystallinity values in the fiber cross-section. (c) all measured crystallinity values in the outmost annulus of the fiber cross-section.

would be possible, by moving the focus point of the laser deeper into the sample. Additionally, Raman maps of fiber samples cut along the fiber axis could reveal interesting microscopic structural changes along the fiber axis. To sum up, high-resolution Raman mapping opens an exciting pathway to study how processing parameters, or other physical and chemical modifications (e.g. plasticizers, crosslinkers), affect the radial structure of polymer fibers.

Author contributions

Raman and AFM (data in brief) measurements have been performed by O. Braun and R. Muff. Sample preparations and ATR-FTIR (data in brief) as well as DSC (data in brief) measurements were performed by K. Sharma and S. Tritsch. K. Sharma has analyzed the DSC (data in brief) data. R. Hufenus has contributed in discussing the manuscript. E. Perret has performed the WAXD, SAXS (data in brief) measurements and has analyzed the Raman, ATR-FTIR (data in brief), WAXD and SAXS (data in brief) data. All authors have contributed to writing the manuscript and have approved the final version of the manuscript.

Funding sources

Data availability

The Raman, WAXD, SAXS, DSC, ATR-FTIR, AFM data are available at DOI: https://doi.org/10.17632/gx9mbxvnf2.1.

CRediT authorship contribution statement

E. Perret: Software, Formal analysis, Investigation, Data curation, Writing – original draft, Visualization. **O. Braun:** Validation, Investigation, Data curation, Writing – review & editing. **K. Sharma:** Methodology, Writing – review & editing. **S. Tritsch:** Methodology, Writing – review & editing. **R. Muff:** Investigation, Data curation. **R. Hufenus:** Supervision, Project administration, Writing – review & editing.

Declaration of competing interest

The authors declare that they have no known competing financial interests or personal relationships that could have appeared to influence the work reported in this paper.

Acknowledgment

References

[1] M. Jaffe, A.J. Easts, X. Feng, 8 - polyester fibers, in: M. Jaffe, J.D. Menczel (Eds.), Thermal Analysis of Textiles and Fibers, Woodhead Publishing, 2020, pp. 133–149.

[2] R. Hufenus, et al., Melt-spun fibers for textile applications, Materials 13 (19) (2020).

[3] R. Hufenus, et al., Bicomponent fibers, in: H. Jinlian, B. Kumar, J. Lu (Eds.), Handbook of Fibrous Materials, Wiley-VCH, Weinheim, Germany, 2018.

[4] J.K. Keum, et al., Orientation-induced crystallization of poly(ethylene terephthalate) fibers with controlled microstructure, Polymer 49 (22) (2008) 4882–4888.

[5] Y. Liu, et al., Lamellar and fibrillar structure evolution of poly(ethylene terephthalate) fiber in thermal annealing, Polymer 105 (2016) 157–166.

[6] T. Toda, H. Yoshida, K. Fukunishi, Structure and molecular motion changes in poly (ethylene terephthalate) induced by annealing under dry and wet conditions, Polymer 36 (4) (1995) 699–706.

[7] E. Perret, et al., Modified crystallization in PET/PPS bicomponent fibers revealed by small-angle and wide-angle X-ray scattering, Macromolecules 46 (2) (2013) 440–448.

[8] N. Chand, U.K. Dwivedi, S.K. Acharya, Anisotropic abrasive wear behaviour of bamboo (Dentrocalamus strictus), Wear 262 (9) (2007) 1031–1037.

[9] P. Kraft, et al., One-dimensional small-angle X-ray scattering tomography of dip-coated polyamide 6 monofilaments, J. Synchrotron Radiat. 17 (2) (2010) 257–262.

[10] N. Stribeck, Analysis of SAXS fiber patterns by means of projections, in: Scattering from Polymers, American Chemical Society, 1999, pp. 41–56.

[11] N. Stribeck, X-ray scattering for the monitoring of processes in polymer materials with fiber symmetry, Polym. Rev. 50 (1) (2010) 40–58.

[12] C.J. Dasch, One-dimensional tomography: a comparison of Abel, onion-peeling, and filtered backprojection methods, Appl. Opt. 31 (8) (1992) 1146–1152.

[13] V. Dribinski, et al., Reconstruction of Abel-transformable images: the Gaussian basis-set expansion Abel transform method, Rev. Sci. Instrum. 73 (7) (2002) 2634–2642.

[14] J. Shimizu, N. Okui, T. Kikutani, Fine structure and physical properties of fibers melt-spun at high speeds from various polymers, in: A. Ziabicki, H. Kawai (Eds.), High-speed Fiber Spinning, John Wiley & Sons, New York, 1985, pp. 429–483.

[15] A. Dazzi, C.B. Prater, AFM-IR: technology and applications in nanoscale infrared spectroscopy and chemical imaging, Chem. Rev. 117 (7) (2017) 5146–5173.

[16] P.N. Tri, R.E. Prud'homme, Nanoscale lamellar assembly and segregation mechanism of poly(3-hydroxybutyrate)/poly(ethylene glycol) blends, Macromolecules 51 (1) (2018) 181–188.

[17] Z. Zhao, et al., Crystallization and microstructure evolution of microinjection molded isotactic polypropylene with the assistance of poly(ethylene terephthalate), Polymers 12 (1) (2020) 219.

[18] S. Biria, I.D. Hosein, Control of morphology in polymer blends through light self-trapping: an in situ study of structure evolution, reaction kinetics, and phase separation, Macromolecules 50 (9) (2017) 3617–3626.

[19] L. Xue, et al., High-resolution chemical identification of polymer blend thin films using tip-enhanced Raman mapping, Macromolecules 44 (8) (2011) 2852–2858.

[20] M. Wang, et al., Distribution of polymorphic crystals in the ring-banded spherulites of poly(butylene adipate) studied using high-resolution Raman imaging, Macromolecules 50 (8) (2017) 3377–3387.

[21] A.A. Leal, et al., Spectroscopic elucidation of structure-property relations in filaments melt-spun from amorphous polymers, Eur. Polym. J. 89 (2017) 78–87.

[22] S. Natarajan, S. Michielsen, Using confocal Raman microscopy to determine the structure and orientation of the PET interior of PET/PP core/shell fibers, Textil. Res. J. 69 (12) (1999) 903–907.

[23] K. Sharma, et al., 2D Raman, ATR-FTIR, WAXD, SAXS and DSC data of PET mono- and PET/PA6 bicomponent filaments (under review), Data in Brief (2021).

[24] R. Hufenus, et al., Biodegradable bicomponent fibers from renewable sources: melt-spinning of poly(lactic acid) and poly[(3-hydroxybutyrate)-co-(3-hydroxyvalerate)], Macromol. Mater. Eng. 297 (1) (2012) 75–84.

[25] R. Nirmala, et al., Effect of solvents on high aspect ratio polyamide-6 nanofibers via electrospinning, Macromol. Res. 18 (8) (2010) 759–765.

[26] E. Perret, et al., X-ray data from a cyclic tensile study of melt-spun poly(3-hydroxybutyrate) P3HB fibers: a reversible mesophase, Data in Brief 25 (2019) 104376.

[27] P.J. Hendra, et al., The application of Fourier transform Raman spectroscopy to the identification and characterization of polyamides—I, *Single number nylons.* Spectrochimica Acta Part A: Molecular Spectroscopy 46 (5) (1990) 747–756.

[28] T. Lippert, F. Zimmermann, A. Wokaun, Surface analysis of excimer-laser-treated polyethylene-terephthalate by surface-enhanced Raman scattering and X-ray photoelectron spectroscopy, Appl. Spectrosc. 47 (11) (1993) 1931–1942.

[29] F.J. Boerio, S.K. Bahl, G.E. McGraw, Vibrational analysis of polyethylene terephthalate and its deuterated derivatives, J. Polym. Sci. Polym. Phys. Ed 14 (6) (1976) 1029–1046.

[30] B.J. Bulkin, M. Lewin, F.J. DeBlase, Conformational change, chain orientation, and crystallinity in poly(ethylene terephthalate) yarns: Raman spectroscopic study, Macromolecules 18 (12) (1985) 2587–2594.

[31] F.J. Deblase, et al., Low-frequency Raman spectra of poly(ethylene terephthalate), J. Polym. Sci., Polym. Lett. Ed. 23 (2) (1985) 109–115.

[32] G. Ellis, et al., FT Raman study of orientation and crystallization processes in poly (ethylene terephthalate), Spectrochim. Acta Mol. Biomol. Spectrosc. 51 (12) (1995) 2139–2145.

[33] N. Everall, et al., Study of density and orientation in poly(ethylene terephthalate) using Fourier transform Raman spectroscopy and multivariate data analysis, Polymer 35 (15) (1994) 3184–3192.

[34] A.J. Melveger, Laser-Raman study of crystallinity changes in poly(ethylene terephthalate), J. Polym. Sci. 2 Polym. Phys. 10 (2) (1972) 317–322.

[35] S.-B. Lin, J.L. Koenig, Spectroscopic characterization of the rotational conformations in the disordered phase of poly(ethylene terephthalate), J. Polym. Sci. Polym. Phys. Ed 20 (12) (1982) 2277–2295.

[36] V. Causin, et al., Forensic analysis of poly(ethylene terephthalate) fibers by infrared spectroscopy, Appl. Spectrosc. 58 (11) (2004) 1272–1276.

[37] K.C. Cole, A. Ajji, É. Pellerin, New insights into the development of ordered structure in poly(ethylene terephthalate). 1. Results from external reflection infrared spectroscopy, Macromolecules 35 (3) (2002) 770–784.

[38] T.R. Manley, D.A. Williams, Structure of terephthalate polymers I—infra-red spectra and molecular structure of poly(ethylene terephthalate), Polymer 10 (1969) 339–384.

[39] S.R. Padibjo, I.M. Ward, A structural study of the tensile drawing behaviour of poly (ethylene terephthalate), Polymer 24 (9) (1983) 1103–1112.

[40] C. Pellerin, M. Pézolet, P.R. Griffiths, Time-resolved infrared spectroscopic studies of poly(ethylene terephthalate) deformation, Macromolecules 39 (19) (2006) 6546–6551.

[41] K.B. Hafsia, et al., A novel approach to study the isothermal and non-isothermal crystallization kinetics of Poly(Ethylene Terephthalate) by Raman spectroscopy, J. Polym. Res. 23 (5) (2016) 93.

[42] B.H. Stuart, Polymer crystallinity studied using Raman spectroscopy, Vib. Spectrosc. 10 (2) (1996) 79–87.

[43] C.C.C. Lesko, et al., Experimental determination of the fiber orientation parameters and the Raman tensor of the 1614cm−1 band of poly(ethylene terephthalate)☆In honour of Professor Giuseppe Zerbi on the occasion of his 65th birthday.☆, J. Mol. Struct. 521 (1) (2000) 127–136.

[44] R. Paquin, M.-H. Limage, P. Colomban, Micro-Raman study of PET single fibres under high hydrostatic pressure: phase/conformation transition and amorphization, J. Raman Spectrosc. 38 (9) (2007) 1097–1105.

[45] E.B. Wilson, The normal modes and frequencies of vibration of the regular plane hexagon model of the benzene molecule, Phys. Rev. 45 (10) (1934) 706–714.

[46] P. Colomban, Analysis of strain and stress in ceramic, polymer and metal matrix composites by Raman spectroscopy, Adv. Eng. Mater. 4 (8) (2002) 535–542.

[47] D.A. Long, Raman Spectroscopy, McGraw-Hill, New York a.o., 1977.

[48] A.I. Abou-Kandil, A.H. Windle, The development of microstructure in oriented polyethylene terephthalate (PET) during annealing, Polymer 48 (17) (2007) 5069–5079.

[49] Y. Fu, et al., Structure analysis of the noncrystalline material in poly(ethylene terephthalate) fibers, Macromol. Chem. Phys. 195 (2) (1994) 803–822.

[50] E.B. Gowd, et al., Effect of molecular orientation on the crystallization and melting behavior in poly(ethylene terephthalate), Polymer 45 (19) (2004) 6707–6712.

[51] S.F. Ran, et al., Mesophase as the precursor for strain-induced crystallization in amorphous poly(ethylene terephthalate) film, Macromolecules 35 (27) (2002) 10102–10107.

[52] J. Purvis, D.I. Bower, I.M. Ward, Molecular orientation in PET studied by polarized Raman scattering, Polymer 14 (8) (1973) 398–400.

[53] D.A. Jarvis, et al., Characterization of biaxial orientation in poly(ethylene terephthalate) by means of refractive index measurements and Raman and infra-red spectroscopies, Polymer 21 (1) (1980) 41–54.

[54] S. Yang, S. Michielsen, Orientation distribution functions obtained via polarized Raman spectroscopy of poly(ethylene terephthalate) fibers, Macromolecules 36 (17) (2003) 6484–6492.

[55] A. Soto, G.A. Voyiatzis, Molecular orientation of poly(ethylene naphthalate)/Poly (ethylene terephthalate) copolymers utilizing polarized Raman spectra, Macromolecules 35 (6) (2002) 2095–2104.

[56] E.J.C. Kellar, et al., Raman vibrational studies of syndiotactic polystyrene. 2. Use of the fundamental ν1 vibrational mode as a quantitative measure of crystallinity within isotropic material, Macromolecules 30 (8) (1997) 2400–2407.

[57] C. Minogianni, K.G. Gatos, C. Galiotis, Estimation of crystallinity in isotropic isotactic polypropylene with Raman spectroscopy, Appl. Spectrosc. 59 (9) (2005) 1141–1147.

[58] A.Z. Samuel, Direct estimation of polymer crystallinity with Raman spectroscopy using ratio of scattering cross-sections estimated from variable temperature measurements, Spectrochim. Acta Mol. Biomol. Spectrosc. 224 (2020) 117431.

[59] R. Androsch, M.L. Di Lorenzo, C. Schick, Optical microscopy to study crystal nucleation in polymers using a fast scanning chip calorimeter for precise control of the nucleation pathway, Macromol. Chem. Phys. 219 (3) (2018) 1700479.

[60] S. Li, et al., Nanoscale morphology, interfacial hydrogen bonding, confined crystallization and greatly improved toughness of polyamide 12/polyketone blends, Nanomaterials 8 (11) (2018).

[61] C. Schick, R. Androsch, Nucleation-controlled semicrystalline morphology of bulk polymers, Poylmer crystallization 1 (4) (2018), e10036.

[62] C. Yu, et al., Crystalline and spherulitic morphology of polymers crystallized in confined systems, Crystals 7 (5) (2017).

[63] C.Y. Li, The rise of semicrystalline polymers and why are they still interesting, Polymer 211 (2020) 123150.

[64] D.A. Ivanov, S.N. Magonov, Atomic force microscopy studies of semicrystalline polymers at variable temperature, in: G. Reiter, J.-U. Sommer (Eds.), Polymer Crystallization: Observations, Concepts and Interpretations, Springer Berlin Heidelberg, Berlin, Heidelberg, 2003, pp. 98–130.

[65] J.Y. Chen, P.A. Tucker, J.A. Cuculo, High-performance PET fibers via liquid isothermal bath high-speed spinning: fiber properties and structure resulting from threadline modification and posttreatment, J. Appl. Polym. Sci. 66 (13) (1997) 2441–2455.

[66] Y.G. Fu, et al., Analysis of structure and properties of poly(ethylene-terephthalate) fibers, J. Polym. Sci. B Polym. Phys. 32 (13) (1994) 2289–2306.

[67] G. Wu, et al., Oriented noncrystalline structure in PET fibers prepared with threadline modification process, J. Polym. Sci. B Polym. Phys. 34 (12) (1996) 2035–2047.

[68] E. Perret, et al., Structural response of melt-spun poly(3-hydroxybutyrate) fibers to stress and temperature, Polymer 197 (2020) 122503.

[69] E. Perret, et al., Tensile study of melt-spun poly(3-hydroxybutyrate) P3HB fibers: reversible transformation of a highly oriented phase, Polymer 180 (2019) 121668.

[70] E. Perret, et al., X-ray Data about the Structural Response of Melt-Spun Poly(3-Hydroxybutyrate) Fibers to Stress and Temperature Data in Brief, vol. 31, 2020, p. 105675.

[71] F. Selli, et al., Mesophase in melt-spun poly(ε-caprolactone) filaments: structure–mechanical property relationship, Polymer 206 (2020) 122870.

[72] F. Selli, et al., Properties, X-ray data and 2D WAXD fitting procedures of melt-spun poly(ε-caprolactone), Data in Brief 32 (2020) 106223.

[73] R.D. Daubeny, C.W. Bunn, The crystal structure of polyethylene terephthalate, Proc. Roy. Soc. Lond. Math. Phys. Sci. 226 (1167) (1954) 531–542.

[74] J. Militky, The chemistry, manufacture and tensile behaviour of polyester fibers, in: A.R. Bunsell (Ed.), Handbook of Tensile Properties of Textile and Technical Fibres, Woodhead Publishing, 2009, pp. 223–314.

[75] T. Kikutani, et al., High-speed melt spinning of bicomponent fibers: mechanism of fiber structure development in poly(ethylene terephthalate)/polypropylene system, J. Appl. Polym. Sci. 62 (11) (1996) 1913–1924.

[76] T. Kikutani, et al., High-speed melt spinning of PET, Int. Polym. Process. 11 (1) (1996) 42–49.

[77] P.D. James Speight, Lange's Handbook of Chemistry, sixteenth ed. sixteenth ed./, McGraw-Hill Education, New York, 2005.

[78] Y.B. Choi, S.Y. Kim, Effects of interface on the dynamic mechanical properties of PET/nylon 6 bicomponent fibers, J. Appl. Polym. Sci. 74 (8) (1999) 2083–2093.

[79] X. Chen, et al., Orientation mapping of extruded polymeric composites by polarized micro-Raman spectroscopy, Journal of Spectroscopy 2015 (2015) 518054.

[80] T. Kochetkova, et al., Combining polarized Raman spectroscopy and micropillar compression to study microscale structure-property relationships in mineralized tissues, Acta Biomater. 119 (2021) 390–404.

[81] E. Perret, R. Hufenus, Insights into strain-induced solid mesophases in melt-spun polymer fibers, Polymer (2021).